

Phase-retrieval analysis of pre- and post-repair Hubble Space Telescope images

John E. Krist and Christopher J. Burrows

Phase-retrieval measurements of point-spread functions from the pre- and post-repair Hubble Space Telescope are presented. The primary goal was to determine the aberrations present in the second wide-field and planetary camera (WFPC2) to align and validate its corrective optics. With both parametric model-fitting techniques and iterative (Gerchberg-Saxton) methods, accurate measurements have been obtained of the WFPC2 and Hubble Space Telescope optics, including improved maps of the zonal errors in the mirrors. Additional phase-retrieval results were obtained for the aberrated, prerepair cameras and the corrected faint-object camera. The information has been used to improve models produced by point-spread-function simulation programs. On the basis of the measurements a conic constant for the primary mirror of $\kappa = -1.0144$ has been derived.

1. Introduction

The successful correction of the spherical aberration present in the Hubble Space Telescope (HST) illustrates the accuracy of the measurements that were used to determine the conic constant of the faulty primary mirror. Of the various methods used by the Hubble Independent Optical Review Panel (HIORP) to quantify the error, phase-retrieval techniques proved to be the most versatile. They provided not only the amount of spherical aberration present but also the coma and the astigmatism, which indicated the alignment of the optical components. Because of its success, phase retrieval was incorporated into plans for tests and alignment both on the ground and in orbit, of the corrective optics of the second wide-field and planetary camera (WFPC2) and of the corrective-optics-space-telescope axial replacement (COSTAR).

We present here the results of the phase-retrieval analyses of WFPC2 images taken as part of the alignment procedure for the servicing-mission observatory-verification program. The primary goal was to measure the residual aberrations present in WFPC2 to verify and to align the corrective optics in the

camera. A secondary goal was to obtain accurate measurements of the zonal errors in the HST optics. These would improve the phase-retrieval fit to the pre- and post-repair camera images and provide a more accurate measurement of the conic constant of the HST's primary mirror. This information would also improve the simulated PSF's produced by programs such as TINY TIM¹ and TIM² (telescope-image modeling), which have been used extensively for deconvolution and data reduction.

2. Overview of WFPC2

The WFPC2 (Fig. 1) consists of four separate cameras that image adjacent sections of the central portion of the HST focal plane. Light from the optical-telescope assembly (OTA) is diverted by a pick-off mirror into the camera. After passing through a set of selectable filters, the light is split into four channels by a reflective pyramid. Each of these beams is reflected by an actuated folding mirror (AFM) into a Cassegrain repeater, which images onto an 800 element \times 800 element Loral CCD with 15.0- μm -square pixels. There are three wide-field channels (WF2, WF3, and WF4) with $f/12.9$ focal ratios and effective pixel sizes of 0.1 arcsec. The other channel is the planetary camera (PC) with an $f/28.3$ focal ratio and a pixel size of 0.0455".

To correct the spherical aberration present in the HST, an image of the OTA's aberrated primary mirror is formed on the secondary mirrors of the repeaters, which have a conic constant that compensates for the error. This procedure has the advantage of needing no additional reflections, as compared

The authors are with the Space Telescope Science Institute, Baltimore, Maryland 21218. C. J. Burrows is also with the European Space Agency, Astrophysics Division, Space Science Department, Estec, 2200 AG, Noordwijk, The Netherlands.

Received 25 July 1994; revised manuscript received 31 October 1994.

0003-6935/95/224951-14\$06.00/0.

© 1995 Optical Society of America.

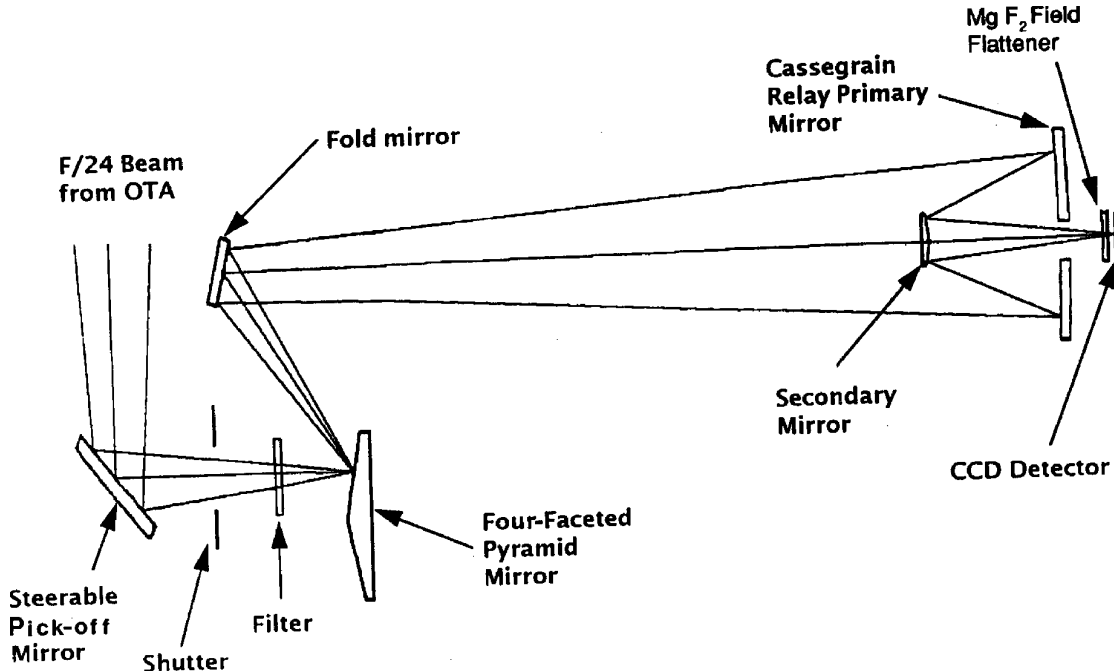


Fig. 1. Schematic diagram of the WFPC2 optical layout.

with the previous, uncorrected camera (WF/PC-1). However, it requires that the camera optics be well aligned, otherwise the pupil will not be properly placed on the secondaries and will result in coma.

To ensure accurate placement of the pupil, the tilts of the AFM's for the PC, WF3, and WF4 channels can be adjusted by means of commands from the ground. The folding mirror for WF2 is fixed because the pick-off mirror, which also tilts, serves to align that channel. An amount of measured coma can be translated into a corresponding tilt error in the mirrors.

The design of the previous camera, WF/PC-1, was similar, except that the folding and pick-off mirrors were fixed and the pyramid rotated to switch between four WFC and four PC repeaters. (We use the acronym WFPC when something applies to both the wide-field and the planetary cameras.)

The initial WFPC2 alignments were based on visual inspection and phase retrieval of in-focus stellar images. A four \times four raster of PSF's was obtained when the pick-off mirror was tilted by predetermined steps, which introduced significant amounts of coma. The setting with the least amount of visible coma was chosen. During alignment, the pick-off mirror was adjusted first so that WF2 was free of coma; then the AFM's were adjusted to align the other channels. Phase retrieval verified the results, but because of the limited spatial frequency and the large dynamic range of the PSF's, the retrieved aberration values were not accurate enough to use for the final alignment. Accurate phase retrieval requires highly defocused PSF's, which are better sampled by the detector in both the spatial and the intensity resolutions.

3. Data

For the final alignment of WFPC2, a series of images of the star HD8538 were obtained with the OTA's

secondary mirror moved from the nominal position by $\Delta_{SM} = \pm 180, \pm 360 \mu\text{m}$ (HST calibration-observation program, proposal no. 5613) (the subscript SM denotes the secondary mirror). Hereafter in this paper, the separation between the primary and secondary mirrors will be referred to as the "despace." A positive despace indicates that the secondary mirror was moved away from the primary. The settings were chosen to be optimal for phase retrieval. Each set of exposures consisted of two images, each taken through narrow-band filters (filters F502N and F953N) at 502 and 953 nm, plus one image taken through a wide-band filter at 170 nm (filter F170W). A set of exposures was taken in the center of each CCD at each mirror position. The PSF's at the extreme settings were approximately 5.5 arcsec in diameter. All sets were well exposed and free from any significant jitter due to the short exposure times of 1–4 s.

The data from filter F170W were not phase retrieved because of the inherent difficulties of retrieval (large array sizes at such short wavelengths and wavelength-dependent effects across the wide passband). As we show below, the information obtained from the other filters was used to generate models that matched the 170-nm data well.

A. Phase Retrieval

We used two different fitting techniques for the WFPC2 data. Parametric phase retrieval (PPR) was used to fit for low-frequency aberrations—defocus, spherical aberration (third and fifth orders), coma, astigmatism, and clover (trefoil) aberration. Iterative, nonparametric phase retrieval (NPPR) was used to obtain higher-frequency errors and to verify the obscuration patterns in the telescope and cameras. Our procedure, which is similar to that described by

Roddier and Roddier,³ was first to fit the PSF's with the PPR procedure to generate an initial wave-front estimate. This estimate provided the starting guess for the NPPR routine, which was based on the Gerchberg-Saxton⁴ (GS) algorithm. The GS procedure then produced a map of the zonal aberrations for which the PPR software could not account with Zernike-type polynomials. The data were again fitted with the PPR program, but now the retrieved error map was included to improve the accuracy of the models.

1. Parametric Phase Retrieval

Software written in the Interactive Data Language was developed to perform the PPR. The program uses either a Levenberg-Marquardt least-squares method or a simplex-fitting procedure to generate PSF models, compare them with the observed data, and then adjust the parameters for the next iteration. The process is repeated until the weighted differences between the squares of the observed and the model PSF's are minimized. We prefer to use the least-squares algorithm because it converges much more rapidly.

The PPR method can account for a number of properties that are difficult or impossible for NPPR methods to incorporate, including jitter, background, field dependence (as a result of obscuration or aberration variability), and detector characteristics. Bad pixels (e.g., cosmic rays or bad columns) can be masked out and given a zero weighting during the data-fitting process.

The PPR program can solve for a wide range of parameters including the Zernike-polynomial coefficients, uniform background level, pixel size, jitter, obscuration positions and sizes, and, if necessary, Gaussian and sloping pupil illuminations. Any parameter can be fitted, fixed at a given value, or ignored. The most important Zernike polynomials are given in Table 1. As is customary in HST optical studies, they are orthonormalized for a 33% central obscuration, which accounts for the OTA's secondary mirror. They can be readily converted to complete

Table 1. Zernike Polynomials Used in the Phase Retrievals

Term	Aberration	Zernike Polynomial
Z_2	x Tilt	$1.89926 \rho \cos(\theta)$
Z_3	y Tilt	$1.89926 \rho \sin(\theta)$
Z_4	Focus	$3.88744 (\rho^2 - 0.5544)$
Z_5	0° Asigmatism	$2.31377 \rho^2 \cos(2\theta)$
Z_6	45° Astigmatism	$2.31377 \rho^2 \sin(2\theta)$
Z_7	x Coma	$8.33456 (\rho^3 - 0.67380\rho)\cos(\theta)$
Z_8	y Coma	$8.33456 (\rho^3 - 0.67380\rho)\sin(\theta)$
Z_9	x Clover (x trefoil)	$2.67017 \rho^3 \cos(3\theta)$
Z_{10}	y Clover (y trefoil)	$2.67017 \rho^3 \sin(3\theta)$
Z_{11}	Third-order spherical	$16.89598 (\rho^3 - 1.10890 \rho^2 + 0.24124)$
Z_{22}	Fifth-order spherical	$74.78245 (\rho^6 - 1.66335 \rho^4 + 0.80314 \rho^2 - 0.10441)$

orthonormal sets over the unobscured aperture or over the WFPC aperture, which has a 42% central obscuration. The radius in the pupil (ρ) is normalized ($0 < \rho < 1$), and in this study the angle is measured from the + $U2$ to the + $U3$ axes in HST coordinates,⁵ which are identical to the ($V2, V3$) pupil, *not* sky, coordinates.

A powerful feature of the software is its ability to fit PSF's simultaneously, even though they are taken at different focus positions. Separate focus terms are fitted for each frame, and separate tilts are fitted for each PSF. The other aberrations are applied to all the PSF's, and corrections are based on ray tracing if an aberration is focus dependent. The focus of the first image frame is specified as the offset of the OTA secondary mirror from the best focus, in micrometers, and the other positions are given as offsets from that frame. If the focus values are known accurately relative to each other, they can be fixed while the position of the first image is fitted to determine the general focus offset.

We have found that simultaneously fitting multiple focus positions significantly constrains many of the parameters. The effects of defocus and spherical aberration are more easily decoupled, especially when images are taken on opposite sides of the focus. The fitting routine is also more sensitive to astigmatism, because the axis of elongation changes 90° through focus. Another benefit (which fortunately was not needed for the on-orbit observations) is the separation of pupil illumination and coma. During thermal-vacuum testing of WFPC2, in which on-orbit alignment procedures were practiced, we found that the intensity of the illumination pattern from the simulated OTA beam increased across the pupil with an approximately Gaussian pattern. The increased intensity caused brightening along one side of the defocused PSF's, and the brightening affected the measured coma when we fitted single PSF's. However, as the system went through focus, the brightening in the PSF that was caused by coma remained on the same side, whereas that caused by the increased intensity in the pupil illumination switched sides. This allowed the program to disassociate the two effects and return accurate coma and pupil-illumination measurements when multiple focus positions were used.

The software also accounts for the variable obscuration patterns in WF/PC-1 and WFPC2. The PSF's in these cameras are field dependent because of the obscurations caused by the repeaters' secondary-mirror support structures (three support struts and the secondary housing). These are not in the plane of the entrance pupil, so depending on field angle they appear to shift relative to the OTA obscurations (which are effectively in the entrance pupil). We have determined the rates of obscuration movement in relation to changes in location on the detector for each camera by ray-tracing the systems. Because the repeater optics are not centered exactly over the middle of each detector, the position at which the

repeater and OTA obscurations are aligned varies with each camera and can be solved for by the software. Multiple field positions can be fitted simultaneously.

The WFPC's obscuration patterns also vary with the focus. As the OTA secondary is moved, the diameter of the beam going into the WFPC repeater changes. This results in an apparent change in the size of the WFPC obscurations (the secondary and spider obscurations) with respect to the pupil diameter. We noticed this effect when we compared the pupil-amplitude maps obtained through the NPPR of the WFPC2 PSF's. For the WFPC2, the measured radius of the PC's secondary obscuration varied from $0.399r$ to $0.435r$ (where r is the pupil radius). We initially used one size for all focus positions and later modified the code to account for the change. The solvable parameters are the sizes of the secondary and the spider obscurations at $Z_4 = 0.0$ and the rate of change in size versus the focus.

Another side effect that results from defocus of the OTA is a change in the spherical aberration in WFPC2. The highly aspheric secondary mirrors in the repeaters are designed to compensate for the aberrated OTA wave front at a specific focus. When the beam diameter changes, the OTA primary mirror no longer maps properly onto the WFPC2 secondary mirrors, and the spherical aberration is not fully corrected. Ray traces of the system predicted that the third-order spherical aberration (Z_{11}) changes by $-1.64 \times 10^{-5} \mu\text{m}$ for each micrometer of the OTA's secondary-mirror despace. Over the $\Delta_{\text{SM}} = \pm 360 \mu\text{m}$ range of focus at which the WFPC2 data were taken, Z_{11} varied by approximately $0.01 \mu\text{m}$. The program accounts for this effect and returns Z_{11} where the focus term (Z_4) is zero.

Our PPR software assumes that all obscurations exist in the same plane, which is not the case for the WFPC cameras. A theoretically more accurate approach would be to compute the diffraction at each plane. It has been stated that the failure to use such a method can cause a significant bias in the measured spherical aberration and other PSF characteristics.⁶ We are not convinced of this consequence and believe that, for the HST, single-plane diffraction models are sufficient because they can measure aberration values to an estimated accuracy of better than $0.003 \mu\text{m}$ rms. Multiple-plane diffraction algorithms themselves require approximations to be practical. However, other factors such as jitter, detector effects, and zonal aberrations are more important. As described below, we have obtained an excellent fit to the observed PSF's by using the single-plane method, and the results are consistent with those reported from the use of multiple-plane algorithms.

To account for sampling by the detector, the pupil-function diameter is adjusted so that the resulting PSF can be rebinned by an integral factor. This adjustment has proven sufficient to fit to data for the defocused WFPC2, the aberrated WF/PC-1, and the faint-object camera (FOC). Explicit integration onto

the detector pixels is an option; one can implement it by convolving the PSF with the ideal-pixel-response function and then sampling the result by using sinc interpolation. Our experiments with fitting defocused PSF's show that the inclusion of pixel integration does not significantly affect the retrieved aberration values ($\Delta Z_{11} < 0.001 \mu\text{m}$), but it does increase the computation time by nearly a factor of 5.

For accurate models, it is necessary to include maps of the zonal errors in the primary and secondary OTA mirrors. These errors are artifacts from the polishing process, and they strongly affect ring intensity and structure, especially in the ultraviolet. Maps obtained from ground-based interferometry of the mirrors were provided by Hughes Danbury Optical Systems and have been used with the PPR software and the TINY TIM and TIM PSF generators for some time. These old maps, however, are inadequately sampled and are apparently not accurate enough to produce models that agree well with the observed PSF's. As described in Section 3.A.1, we have obtained a better zonal map using the NPPR method on the WFPC2 data and have incorporated it into the PPR software.

2. Nonparametric Phase Retrieval

Although the PPR software can be used to fit the low-frequency (Zernike-type) aberrations, it cannot solve for the midfrequency aberrations caused by the zonal errors. These must be obtained with the iterative, NPPR methods, such as the GS procedure. We used the GS procedure to obtain the improved mirror map and to verify the obscuration positions and sizes. The WFPC2 PSF's at 502 nm were the most thoroughly analyzed because the effects of the zonal errors at that wavelength are greater than those at 953 nm. The 170-nm data were not used because of the wide passband of the filter, possible aliasing of the retrieved wave front at short wavelengths, and the large array sizes required.

The GS algorithm begins with an initial guess of the wave-front and pupil amplitudes. This complex pupil function is Fourier transformed into image space to form the complex amplitude. The modulus of the complex amplitude is divided out and replaced by the observed amplitude, which is simply the square root of the observed PSF. The result is Fourier transformed back, and constraints are placed on the pupil amplitude on the basis of the known obscuration sizes and positions. This process is reiterated until the computed PSF converges.

In our analyses, we generated the initial wave-front estimate by summing the Zernike polynomials with the coefficients determined from fitting the PPR data. During verification of the obscuration positions and sizes, the only initial constraint on the pupil amplitude was that all values outside of the pupil be set to zero. After approximately 5 to 10 iterations, the retrieved amplitude was defined well enough so that we could accurately measure the obscurations (Fig. 2).

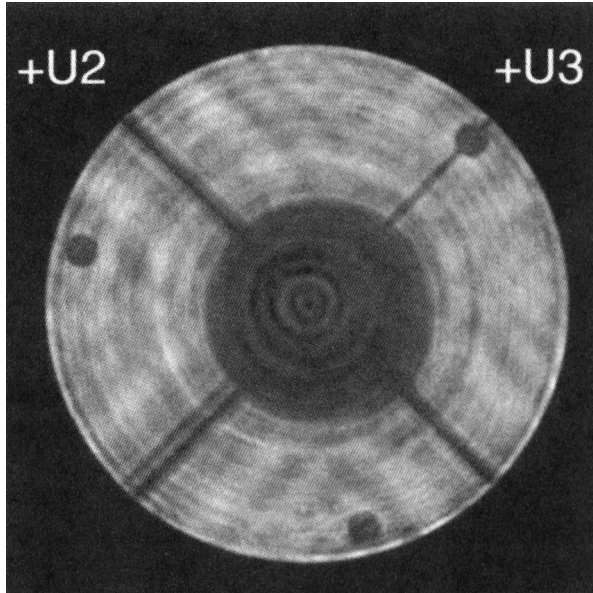


Fig. 2. Pupil amplitude in the WFPC2 PC derived from 15 GS iterations and constrained only outside the pupil.

A peculiarity of NPPR methods is that, unless adequately constrained, they will produce anomalous patterns in the pupil amplitude. As the image in Fig. 2 shows, ripples formed around the spiders, and rings formed around the mirror-support pads and inside the central obscuration. The rings in the center proved useful to ensure that the tilt terms were correct because they became distorted and nonconcentric when the wave front was not properly centered. In addition to the use of the rings, the tilt terms were adjusted by comparison of the OTA spider patterns (which are fixed in the entrance pupil) in the images predicted for the pupil with those in the retrieved one. Except for the sharp, dark areas caused by the obscurations, most of patterns were not physical but were instead artifacts of the GS algorithm.

After verifying that the predicted obscuration pattern was correct, we reran the GS routine. In the first 15 iterations, the retrieved pupil amplitude was replaced with the predicted one (suitably scaled in throughput), which enforced completely dark obscurations and a constant illumination. In subsequent iterations the only constraint was that values outside of the pupil were zeroed. After a total of 50 iterations, the fitting values had usually converged. The resulting pupil amplitude was far more uniform than that generated by the initial run, with only high-frequency structures remaining in the unobscured areas. Most of these structures appeared to be associated with the zonal errors, and Roddier and Roddier³ have suggested that they may be caused by light being scattered outside of the pupil by the zones.

To obtain the residual error, we subtracted the initial wave-front estimate from the retrieved wave front. Both of these arrays were phase wrapped. Because the GS routine did not make any large changes to the low-frequency aberrations and be-

cause the aberrations were small, no explicit phase unwrapping was necessary. Points that did not unwrap during subtraction and that had values above $+\pi$ or below $-\pi$ that were due to changes made in the wave front (usually by the zonal errors) were adjusted by the addition of -2π or $+2\pi$, respectively.

The residual wave front was fitted for low-frequency aberrations, which produced a set of Zernike coefficients. These were added to the input wave-front estimate, and the GS process was again repeated. This procedure was iterated until all of the fitted coefficients were below 0.001 μm . At this point the residual wave front could be used as a map of the zonal errors on the mirrors. This map replaced the one used with the PPR software, which was again used to obtain new coefficients for input to the GS routine. The entire PPR-NPPR-PPR process was repeated until the coefficients measured by the PPR software produced less than 0.001 μm of any Zernike aberration in the residual wave front.

There are NPPR methods, such as the Missell algorithm,³ that use two or more PSF's taken at different focus positions and iterate back and forth between them. In pupil space, the wave front retrieved from one PSF is multiplied by a focus-correction term and transformed into the image space of the other PSF. These algorithms require that the pupil amplitudes for all the PSF's be the same, but, as that was not the case for our data, we did not use such methods.

B. Revised Zonal-Error Map

For each focus position, a mirror map was obtained with the process described in Section 3.A. The PC data from 502 nm at the $\Delta_{\text{SM}} = \pm 360 \mu\text{m}$ positions were the most useful because of the high resolution across the PSF's and the pronounced effects of the zonal errors at that wavelength. At 953 nm, where the errors are less significant, the maps were of low contrast and showed only the largest zones. The wide-field-camera maps agreed well with those from the PC, but the lower sampling resulted in reduced resolution. There was no indication of any significant zonal errors in the WFPC2 repeater optics, and the maps were consistent across the focus.

We constructed a master mirror map by averaging the PC maps from 502 nm. Because the PC secondary obscuration was smallest at $\Delta_{\text{SM}} = +360 \mu\text{m}$, the maps from that position revealed slightly more of the inner section of the mirror than did those from the other position, so they replaced the average in that region. The remaining central area affected by the WFPC2 secondary obscuration at the field center was filled in from the old maps. Portions that were obscured by the WFPC2 spiders were replaced with data spliced from neighboring regions.

The master map is valid only for WF/PC-1 and WFPC2 because they view the OTA secondary mirror on axis. The off-axis instruments, such as the FOC, view different portions of that mirror, and thus the structures in the secondary mirror appear shifted

relative to those in the primary. Because we did not have a separate, revised secondary-mirror map, we used the old one. This was certainly not ideal because the resolution of our phase-retrieved map was approximately 3 times that of the old one in each dimension. We fitted Zernike polynomials to the secondary-mirror map before using it and found no significant low-frequency aberrations. The old map was then subtracted from the new map to create an estimate of the primary errors. For off-axis instruments, the PPR and PSF generators shift the secondary errors appropriately and then add them to the primary errors.

The old and new maps are shown in Fig. 3. The general placement and relative intensities of the major features agree well. Figure 4 is a plot of the azimuthal average of one quarter of the maps. The rms wave-front error that is due to the zonal errors is $0.018 \mu\text{m}$, and the minimum and maximum surface errors are -0.054 and $+0.040 \mu\text{m}$. The most obvious differences between the old and new data are the gains in resolution and contrast in the new map, which reveal a finer structure not visible in the old data. Many of the rings have broken into separate ones, and some pits in the mirror have become more pronounced. The old map's resolution was 17.2 mm on the primary, whereas that of the new one is 8.8 mm .

C. Results for WFPC2

The phase-retrieval measurements of the WFPC2 images are presented in Table 2 and shown in Fig. 5. Each aberration value is the average of the two measurements taken in each camera and filter. The Z_{11} value is specified at the best focus for each camera ($Z_4 = 0.0$), and the focus values are derived from sharpness measurements (described below). The results indicated that approximately $0.006 \mu\text{m}$ rms of coma was still present in the PC, WF3, and WF4 cameras. The coma at 953 nm was consistently greater than that at 502 nm by approximately $0.008 \mu\text{m}$ along a common axis. We determined that this was due to slight differences in the wedges of the filters, which would cause shifts in the location of the pupil on the WFPC2 secondaries, resulting in coma. The amount and direction of the differences between the two filters agreed with that computed from the wedges measured during the construction of WFPC2. The AFM's were adjusted for zero coma for the average wedge. The WF2 coma was negligible, so no change was made to the pick-off mirror tilt. Even with the measured coma, the wave-front errors in all of the cameras were below the specified design budget.

The total remaining rms wave-front errors after coma had been zeroed out (except in WF2) are (including defocus): 0.052 , 0.060 , 0.063 , and $0.075 \mu\text{m}$ for the PC, WF2, WF3, and WF4, respectively. The largest remaining aberrations are defocus, spherical aberration, and astigmatism. The scatter in the astigmatism values makes it difficult to determine if

the primary source is in the camera or in the OTA, although the WFPC2 prescription indicates that nearly $0.01 \mu\text{m}$ of astigmatism is inherent in the instrument. Most of the spherical aberration, as we discuss in Section 3.D, appears to be attributable to a slight error in the conic constant to which WFPC2 was built. Data fitting returned a consistent fifth-order spherical aberration (Z_{22}) of approximately $0.003 \mu\text{m}$.

The PC PSF's from filter F502N for the four focus positions were fitted separately to determine the spread in Z_{11} values. The obscuration and spherical-aberration dependencies of focus were included. The fittings returned $Z_{11} = -0.0135$, -0.0122 , -0.0131 , $-0.0136 \mu\text{m}$ for the $\Delta_{\text{SM}} = -360$ through $+360 \mu\text{m}$ settings, respectively.

One aberration we had expected would be present was clover (trefoil) since the three pads that hold the OTA primary in place are expected to stress it to some degree. Although our results indicated the presence of clover above the expected error of measurement, there was some scatter in the values among the repeaters. Because the mirrors in the repeaters have three-point supports, they may introduce clover separately. We estimate the clover aberration in the OTA to be approximately $0.007 \mu\text{m}$ in both x and y .

We verified the dependence of the Z_{11} spherical aberration on the focus by individually fitting the WFPC2 PC 502-nm PSF's from the extreme-focus positions. The Z_{11} term was not adjusted for focus. The retrieved Z_{11} values were -0.0195 and $-0.0076 \mu\text{m}$ at $\Delta_{\text{SM}} = +360$, $-360 \mu\text{m}$, respectively. These values correspond to a change in Z_{11} of $-1.65 \times 10^{-5} \mu\text{m}$ for each micrometer of OTA secondary defocus, which compared well with the predicted value mentioned above.

The results also provided a separate determination of the differences in focus among the WFPC2 repeaters. Measurements made during the thermal-vacuum tests and the on-orbit observations indicated that the repeaters are not precisely confocal. We determined the offsets between cameras by moving the telescope (or simulator) through focus and then computing the median sharpness at each setting. "Sharpness" is defined as the sum of the squares of the values of an intensity-normalized PSF, and it peaks at the best focus. We have found this statistic to be a sensitive measure of focus in undersampled, well-corrected systems such as WFPC2. The median sharpness is computed with a number of stars from an image of a cluster to account for the effects of PSF positioning within a pixel. The optimal focus for each camera was derived when a curve was fitted to the sharpness-versus-focus distribution. We believe that the offsets determined using this technique are more accurate than those derived from phase retrieval because numerous data points are measured at each focus. The offsets (from sharpness) of the WF2-WF4 cameras from the PC are equivalent to the OTA secondary-mirror despaces of 6.8 , 10.6 , and $8.0 \mu\text{m}$, respectively. These translate to wave-front

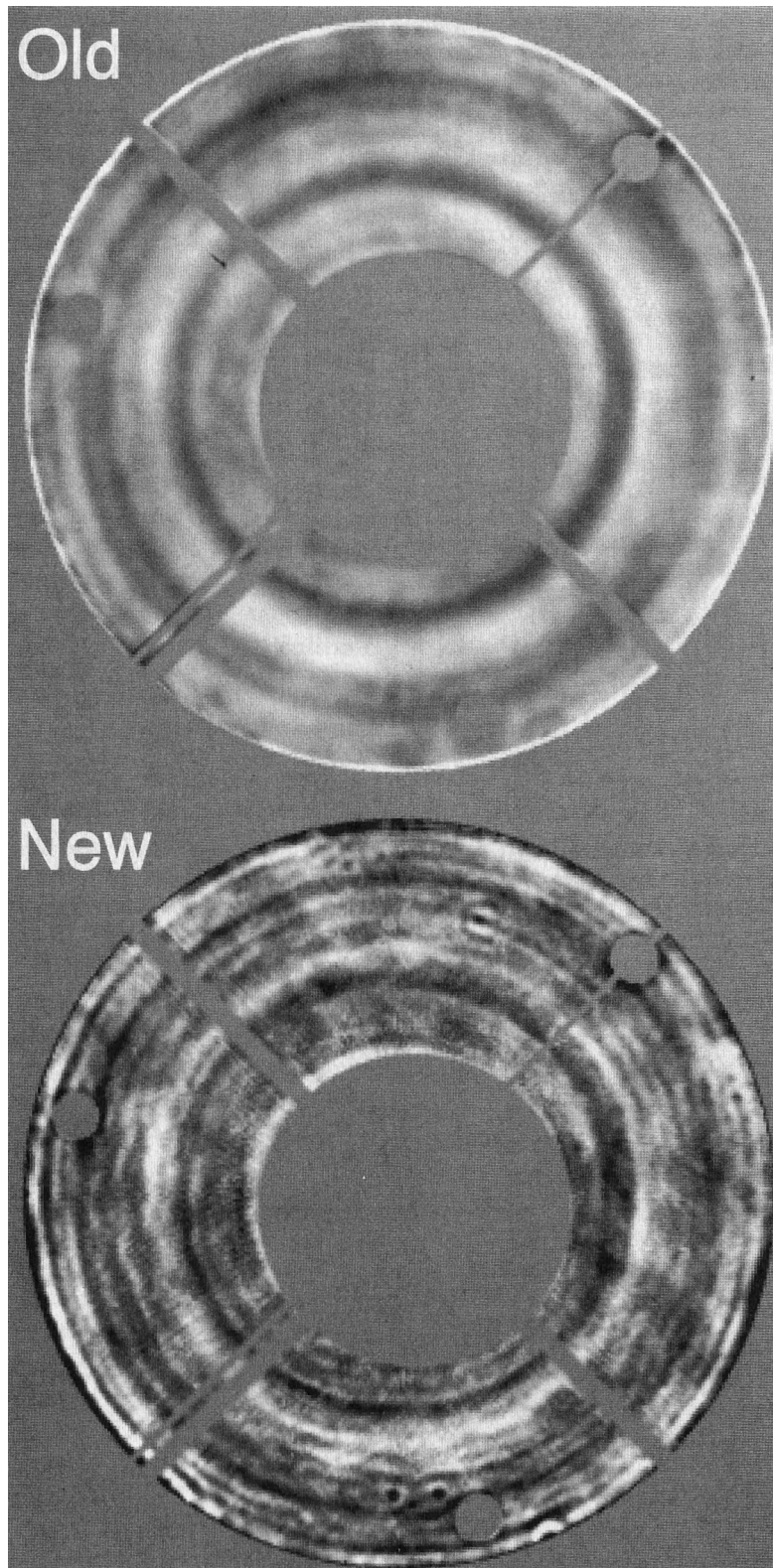


Fig. 3. Mirror zonal-error maps scaled between $\pm 0.03 \mu\text{m}$ of the surface error with WFPC2 and OTA obscurations superposed.

focus errors of $Z_4 = 0.041, 0.064, 0.048 \mu\text{m}$, respectively. The corresponding offsets obtained from phase retrieval are 3.3, 7.7, and 5.5 μm ($Z_4 = 0.020, 0.047, 0.033 \mu\text{m}$). The latter values differ by

$\Delta_{\text{SM}} \approx 3 \mu\text{m}$ from those determined with the sharpness. This difference may be an artifact of breathing, which is a thermally induced change in focus that occurs within the span of an orbit that typically has

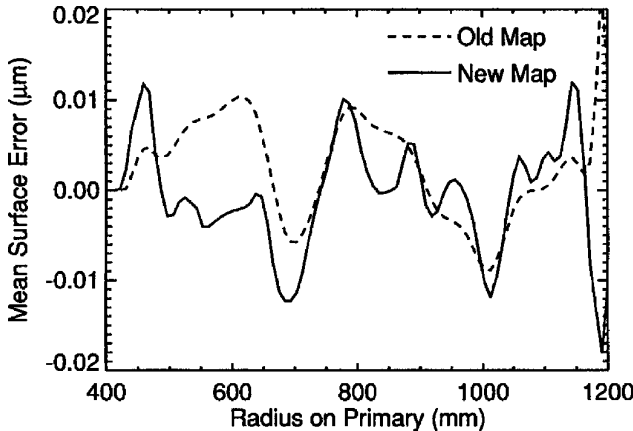


Fig. 4. Azimuthal averages plotted for a one-quarter section of the old and new zonal-error maps.

an amplitude of $\Delta_{SM} \approx 5 \mu\text{m}$. The PC data may have been taken when the telescope focus was affected by breathing (the data for each camera were taken at the same orbital phase). Because the cameras cannot be individually adjusted for focus on orbit, the telescope's secondary mirror is positioned to provide the best image in the PC. The measured focus range agreed to within 1% of the commanded secondary-mirror moves.

Fitting also provided the apparent WFPC2 obscuration sizes and positions at the nominal focus. The diameter of the PC secondary obscuration is $0.410r$ and the spiders are $0.058r$ wide (r is the pupil radius). The WFC secondaries are $0.433r$ in diameter and the spiders are $0.048r$ wide. The (x, y) pixel-coordinate positions on the detectors at which the WFPC2 obscurations appeared to be aligned with those of the OTA are $(380, 428)$, $(432, 398)$, $(395, 400)$, and $(390, 400)$, for the PC and WF2–WF4, respectively. These positions were checked by examination of the flat fields in each camera. Because of the apparent movement of the obscurations, the vignetting pattern in the flat fields includes a bright cross where the

WFPC2 and OTA spiders are overlaid (i.e., where less light is being blocked). The alignment centers determined from the flat fields agreed with those from the phase retrievals.

Although the images taken through filter F170W were not fitted, we generated models for that filter using the TINY TIM program (Fig. 6). The filter-F502N aberrations were used (the coma differences that were due to filter wedges were disregarded). The models show that the structure that results from the zonal errors dominates the PSF, and the new map derived from the 502-nm data can be used at shorter wavelengths.

D. Phase Retrieval of PSF's from the Aberrated Cameras and from COSTAR

With the increased fidelity of the models that resulted from the improved mirror map, we decided to fit the PSF's from the uncorrected WF/PC-1 and FOC cameras, as well as the COSTAR-corrected FOC. Our goals were to obtain accurate aberration values to be used by the PSF generators, to verify the reliability of the new map, and to revise the conic constant of the OTA primary using these measurements and those from WFPC2.

Defocused PSF's from the PC5 and PC6 cameras of WF/PC-1 were extracted from the Space Science Telescope Institute's HST archive. These were part of the Hubble Aberration-Recovery Program (HARP) that was initiated by the HIOPR. The PC5 data were taken at $\Delta_{SM} = -300 \mu\text{m}$ (image W0B16104T) and $+333 \mu\text{m}$ (image W0B17104T) through filter F547M. The PC6 data were taken at $-260 \mu\text{m}$ (image W0BT0802T) and $+250 \mu\text{m}$ (image W0BT0302T) through filter F486N and at $-267 \mu\text{m}$ (image W0DI0402T) and $+210 \mu\text{m}$ (image W0DI0B03T) through filter F889N. The two PSF's in each filter were fitted simultaneously.

The WF/PC-1 fits were excellent and further validated the accuracy of the retrieved mirror map, as shown in Fig. 7. The Z_{11} terms for the two PC6

Table 2. Measured rms Aberrations (μm) in the (U_2, U_3) Coordinates

Error	Camera and Filter Designations							
	PC		WF2		WF3		WF4	
	502 nm	953 nm	502 nm	953 nm	502 nm	953 nm	502 nm	953 nm
Aberration errors (Term)								
Defocus (Z_4)	0.0000	0.0000	0.0410	0.0410	0.0640	0.0640	0.0480	0.0480
0° Astigmatism (Z_5)	0.0201	0.0256	0.0124	0.0094	0.0116	0.0136	0.0186	0.0139
45° Astigmatism (Z_6)	0.0088	0.0121	0.0017	0.0064	0.0115	0.0110	0.0197	0.0182
V_2 Coma (Z_7)	0.0023	-0.0024	0.0021	0.0003	-0.0014	-0.0059	-0.0061	-0.0119
V_3 Coma (Z_8)	-0.0057	-0.0106	-0.0047	-0.0074	-0.0044	-0.0155	0.0058	-0.0020
x Clover (Z_9)	0.0062	0.0063	0.0123	0.0118	0.0012	0.0007	0.0096	0.0095
y Clover (Z_{10})	0.0024	0.0021	0.0075	0.0107	0.0148	0.0112	0.0041	0.0043
Spherical (Z_{11})	-0.0132	-0.0129	-0.0217	-0.0213	-0.0265	-0.0264	-0.0253	-0.0241
Fifth-order spherical (Z_{22})	0.0034	0.0034	0.0035	0.0032	0.0035	0.0036	0.0034	0.0023
Zonal errors	0.0180	0.0180	0.0180	0.0180	0.0180	0.0180	0.0180	0.0180
Total root-sum-square errors	0.0394	0.0476	0.0551	0.0551	0.0769	0.0784	0.0702	0.0672
Design-budget allowance	0.0813	0.0813	0.0794	0.0794	0.0794	0.0794	0.0794	0.0794

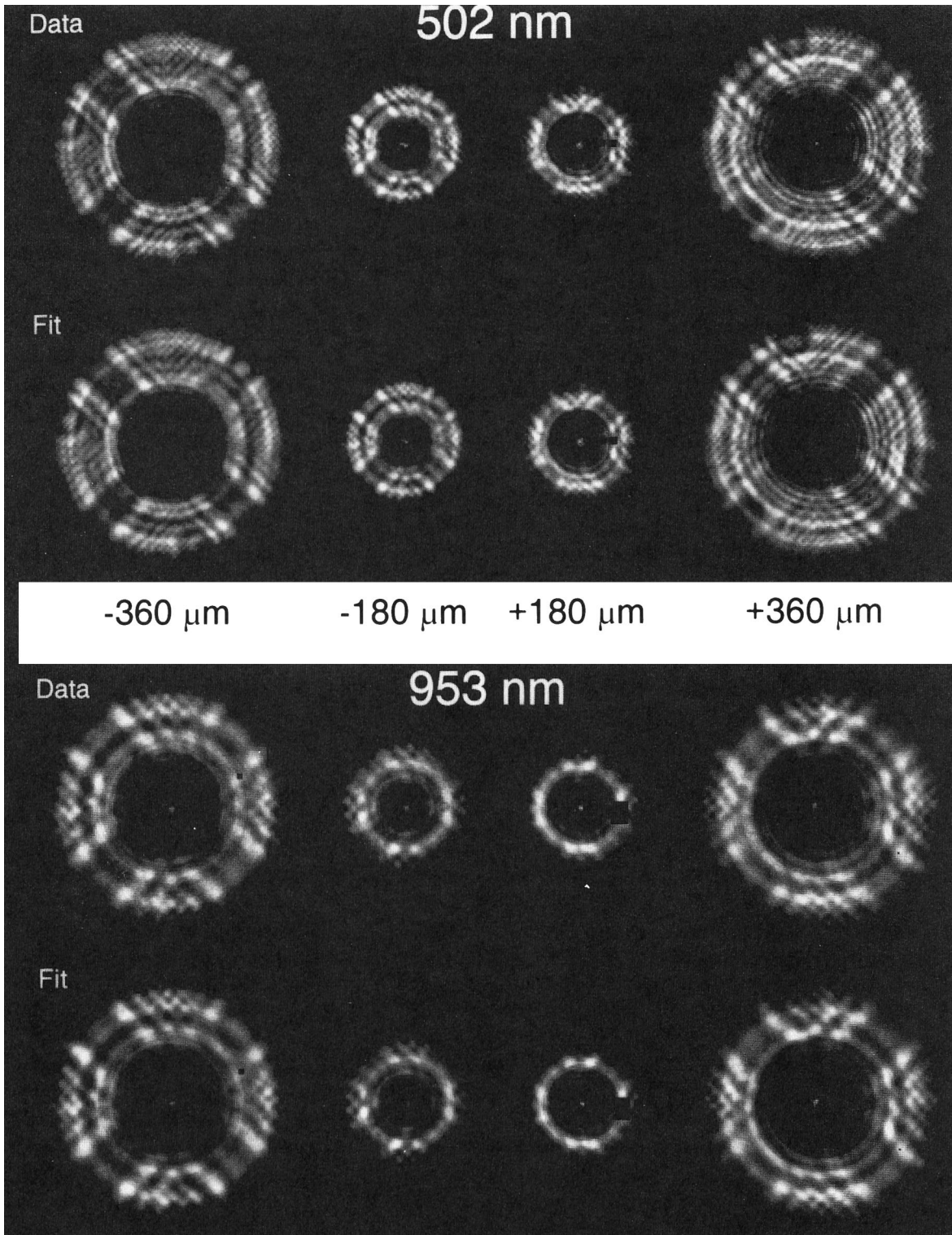


Fig. 5. Data and the corresponding fitted images from the PC of WFPC2.

fittings were consistent to within $\pm 0.001 \mu\text{m}$. The difference in spherical aberration between PC5 and PC6 is probably real, given the quality of the data fit and the measured variances among the similar WFPC2 repeaters.

The PC6 Z_{11} value returned by our software was

equal to that obtained by Fienup *et al.*⁶ using multiple-plane diffraction phase retrieval on the same filter-F889N PSF's. Fienup *et al.*⁶ reported that single- and multiple-plane fits returned $Z_{11} = -0.28, -0.299 \mu\text{m}$, respectively, and used this difference to argue that single-plane diffraction was insufficient to pro-

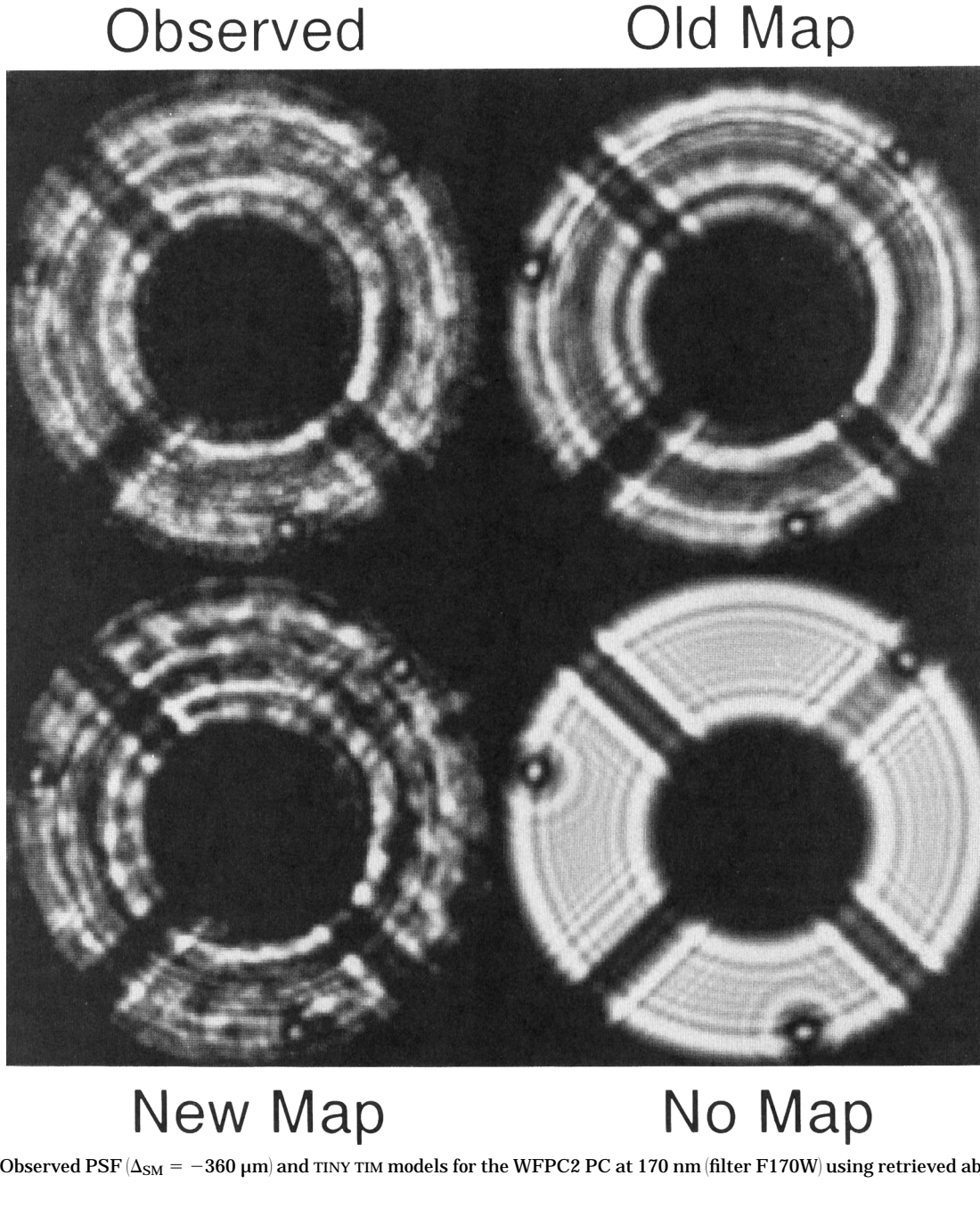


Fig. 6. Observed PSF ($\Delta_{SM} = -360 \mu\text{m}$) and TINY TIM models for the WFPC2 PC at 170 nm (filter F170W) using retrieved aberrations.

duce accurate models. It is possible, however, that when they fitted their single-plane data they encountered a local minimum, given the agreement between the multiple-plane fitting results and our single-plane ones. Other phase-retrieval studies^{3,7,8} that employed single-plane models have reported the same value as ours. We are convinced by the consistency and agreement in our results that single-plane diffraction models are sufficient for the use in the HST phase-retrieval, optical-studies, and deconvolution. The Z_{11} values obtained from WF/PC-1 and WFPC2 agreed with those from the FOC, which does not introduce any additional obscurations.

In-focus, pre-COSTAR, FOC PSF's taken through filters F253M, F307M, and F486N were also analyzed.

Images for the first two filters were obtained from a library of observed PSF's at the Space Telescope Science Institute. They had unusually high signal-to-noise ratios for FOC PSF's. The image from filter F486N was from an HST calibration-monitoring program. The fit (Fig. 8) was generally good, although, because of noise and the limited dynamic range in the wings, the results are likely to be less accurate than those obtained from WF/PC-1 or WFPC2. Because these PSF's were taken at shorter wavelengths than those from WF/PC-1, the effects of the zonal errors were more evident, and some discrepancies that are due to the lack of a good secondary-mirror map were both expected and observed. Still, the combined new and old maps significantly improved the fits and

Observed

Model

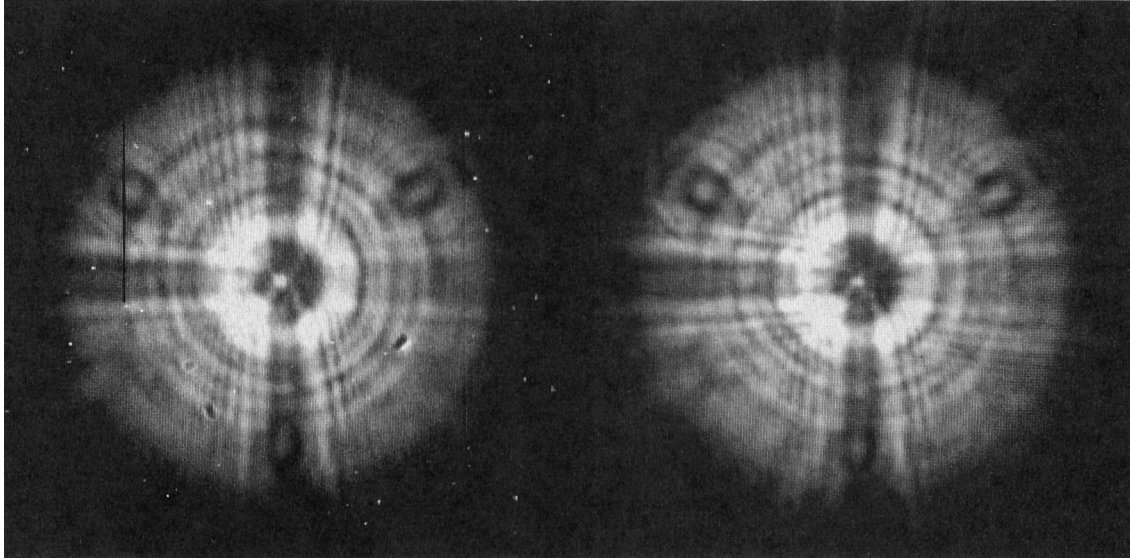


Fig. 7. Fitted data to the WF/PC-1 PC6, filter F486N PSF ($\Delta_{SM} = -260 \mu\text{m}$). The observed PSF includes cosmic rays, dust artifacts, and bad CCD columns.

permitted, for the first time, accurate phase retrieval on such short-wavelength PSF's from the HST. The Z_{11} values derived from these PSF's were constant to within $\pm 0.001 \mu\text{m}$ across the wavelength range.

COSTAR-corrected FOC PSF's through filter F486N were also obtained. These were originally used to verify the final COSTAR alignment, as no COSTAR-corrected FOC images were taken with the OTA significantly defocused. Like the WFPC2 measurements, they indicated a slight residual amount of spherical aberration ($Z_{11} = -0.0085 \mu\text{m}$).

4. Improved PSF Models

Until this study, the simulated PSF's produced by programs such as TINY TIM and TIM were either poor or fair matches to the observed ones because the structure resulting from the zonal errors was not well reproduced with the old maps. The mismatches were evident in side-by-side comparisons, although at longer wavelengths ($\lambda > 700 \text{ nm}$) the agreement was better because of the reduced effects of the zonal errors. The PSF errors resulted in poor deconvolutions that had residual structures that could have been misinterpreted as astronomical features.

To examine the importance of various parameters on the quality of the PSF fit, we executed a series of phase retrievals on the WFPC2 PC data from filter F502N. Some additional parameters were added to each fitting procedure. As shown in Table 3, including the zonal errors resulted in the greatest improvement, whereas adjusting the obscuration size on the basis of focus produced the largest change in the Z_{11} spherical-aberration term. Fittings with the old map included the spherical aberrations that were present in the map ($Z_{11} = 0.0045 \mu\text{m}$ and $Z_{22} = 0.0096 \mu\text{m}$).

5. Revised Primary-Mirror Conic Constant

The HST's primary mirror was intended to have a conic constant of $\kappa = -1.0022985$. After the discovery of the spherical aberration,⁸ NASA created the HIOPR⁹ (see Section 1) to designate the conic constant to use to build the corrective optics. The initial determination was $\kappa = -1.0135$ ($Z_{11} = -0.254 \mu\text{m}$), which was a compromise between higher values ($\kappa \approx -1.0142$) from phase-retrieval studies and lower values ($\kappa \approx -1.0133$) from measurements of the faulty test equipment used to test the mirror. WFPC2 was built to this initial value to meet its schedule. COSTAR was built to the panel's final value, $\kappa = -1.0139$ ($Z_{11} = -0.263 \mu\text{m}$), which was pushed higher by revised measurements of the test equipment.

Our results for WFPC2 indicated that the compromise conic constant derived by the HIOPR underestimated the spherical aberration by a small but measurable amount. Assuming that the value was unknown, we used the spherical measurements from the thermal-vacuum tests to derive an absolute Z_{11} baseline. In those tests, a stimulus was used to simulate the aberrated OTA. We measured the Z_{11} coefficient of the stimulus alone and another group (the Independent Verification Team) did the same; the two measurements were -0.2585 and $-0.2542 \mu\text{m}$, respectively. We used the mean of the two values, $Z_{11} = -0.2563$. Our phase-retrieval results for the cameras with the stimulus were $Z_{11} = 0.0006, -0.0057, -0.0089, -0.0089 \mu\text{m}$ for the PC, WF2, WF3, and WF4, respectively. The cameras exhibited the same variations in Z_{11} in the test as they did on orbit. Computing the difference between the on-orbit and thermal-vacuum test measurements and accounting

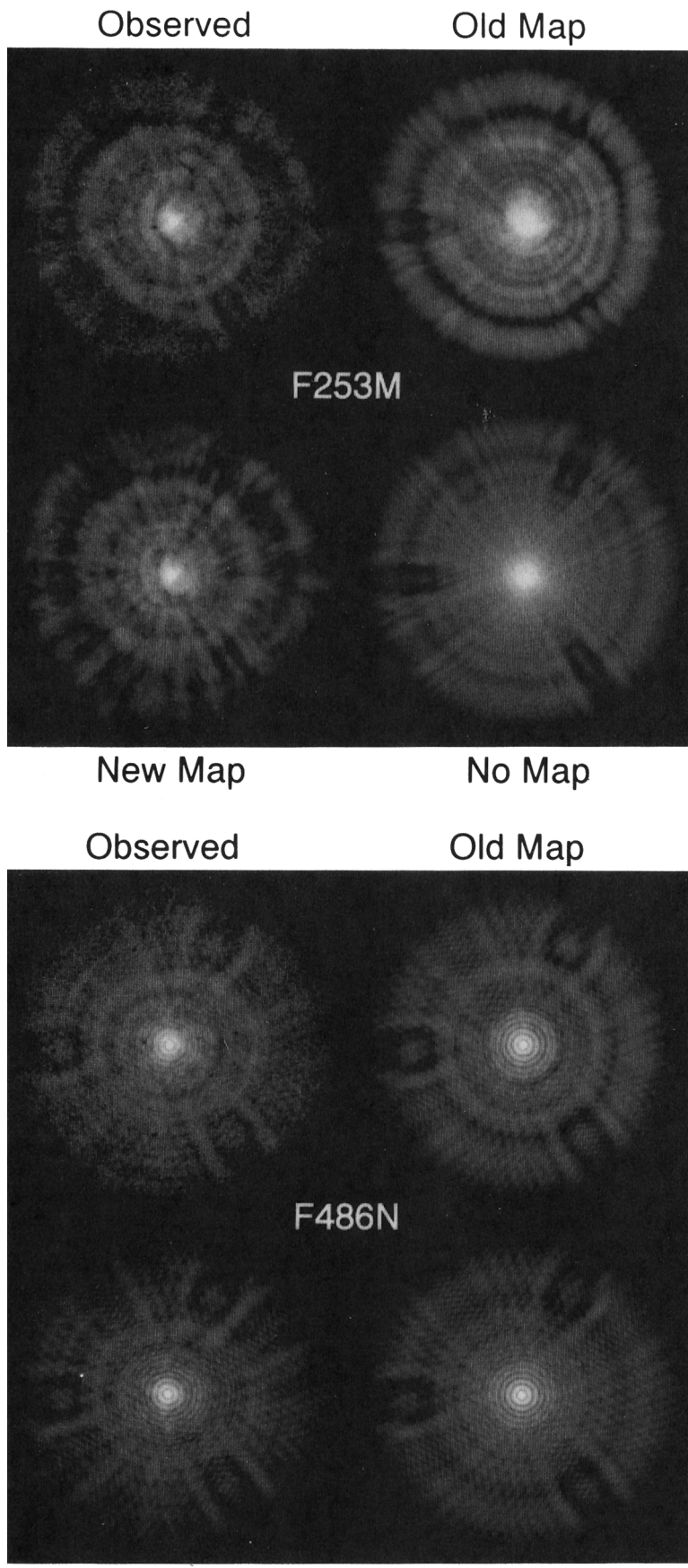


Fig. 8. In-focus FOC ($f/96$) observed and TINY TIM model PSFs (prerepair) with aberrations determined from the phase retrieval.

Table 3. Effect of Additional Terms on the Fitting Parameters and the Quality of Fit

Parameter Combinations	Z_{11} (μm)	Z_{22} (μm)	Data-Fit (rms)
Focus, Z_{11} spherical aberration, and tilt	-0.0038		0.2678
Focus, Z_{11} spherical aberration, and tilt, plus:			
Obscuration size change	-0.0094		0.2663
Coma and astigmatism	-0.0093		0.2641
Clover and Z_{22} spherical aberrations	-0.0118	0.0064	0.2556
Old zonal-error map	-0.0150	-0.0057	0.2180
New zonal-error map	-0.0132	0.0034	0.1020

for the stimulus' conic constant, we found the OTA conic constant derived from the average of the WFPC2 data to be $\kappa = -1.0143 \pm 0.0001$. The conversion from Z_{11} to κ is (Furey¹⁰)

$$\kappa = -1.00223 + \frac{\frac{Z_{11}}{0.6328} + 0.0256\delta}{35.30},$$

where Z_{11} is in micrometers and δ is the offset of the OTA secondary in millimeters from the secondary-to-primary mirror spacing (4906.8869 mm) which puts the paraxial focus at the detector ($\delta = +0.13$ mm). A positive offset indicates that the separation is greater.

The FOC camera is supposedly free of spherical aberration, so a Z_{11} measured in it should directly determine the OTA's conic constant. From our re-

Table 4. Measured Spherical-Aberration (Z_{11}) Values and the Corresponding Conic Constants

Camera	λ (nm)	Z_{11} (μm)	Conic Constant κ
FOC ($f/96$)	253	-0.275	-1.0144
	307	-0.278	-1.0146
	486	-0.279	-1.0146
	486	-0.298	-1.0145 ^a
PC6	889	-0.301	-1.0146 ^a
WFPC2	502	-0.013	-1.0142 ^b
	953	-0.013	-1.0142 ^b
	502	-0.019	-1.0143 ^b
	953	-0.020	-1.0143 ^b
WF3	502	-0.023	-1.0144 ^b
	953	-0.025	-1.0144 ^b
	502	-0.022	-1.0143 ^b
	953	-0.023	-1.0143 ^b
WF4	486	-0.009	-1.0143 ^c
COSTAR plus FOC ($f/96$)			
Mean			-1.0144

^aAdjusted for the spherical aberration in PC6.

^bAdjusted with repeater Z_{11} values from the thermal-vacuum tests.

^cAssumed COSTAR was designed to $\kappa = -1.0139$.

sults, $Z_{11} = -0.277 \pm 0.002$ μm, which corresponds to $\kappa = -1.01445 \pm 0.0001$.

The conic constant derived from the WF/PC-1 data is more uncertain because the repeaters in the WF/PC-1 contain varying amounts of spherical aberration and there is no baseline measurement. The HIOPR adopted a value of $\Delta\kappa = -0.001$ ($\Delta Z_{11} = -0.022$ μm) for the PC6 repeater alone that was based on interferograms obtained during construction. Using this value, we obtained a mean Z_{11} value for PC6 (including the OTA) of -0.300 ± 0.001 μm, which indicates that $\kappa = -1.0146 \pm 0.0002$.

Finally, the value for COSTAR plus the FOC of $Z_{11} = -0.0085$ μm corresponds to $\kappa = -1.0143$, if we assume that COSTAR was built correctly, as specified, for $\kappa = -1.0139$. The results are summarized in Table 4. The mean of these values is $\kappa = -1.0144$, which is close to the phase-retrieval results reported to the HIOPR. The differences between this result and the officially designated conic constant (-1.0139) are not significant for the current HST instruments.

6. Conclusions

We have obtained accurate measurements of the aberrations present in the HST cameras, from both before and after the servicing mission that installed the corrective optics. Our results indicate that WFPC2 is within its designated wave-front error budget, although a small amount of residual third-order spherical aberration is present. The excess spherical aberrations measured in WFPC2 and in COSTAR plus the FOC indicate that the conic constant of the telescope as designated by the HIOPR was underestimated. Phase retrieval values of the aberrated PSFs from WF/PC-1 and from the FOC also favor a greater conic constant, with the new value's being $\kappa = -1.0144$.

A new map of the zonal errors that are present in the primary and secondary mirrors was obtained, with improved contrast and resolution when compared with the map derived from ground-based, pre-launch tests. The new map significantly improves PSF models and appears to be consistent across wavelength and focus ranges and cameras. The old secondary-mirror map can be used with the new combined map to provide models for off-axis instruments, such as the FOC.

This work was funded by the Wide-Field and Planetary Camera Investigation Definition Team (NASA contract NAS7-1260). The study was based on observations made with the NASA/European Space Agency Hubble Space Telescope. Measurements were obtained from the Space Telescope Science Institute, which is operated by the Association of Universities for Research in Astronomy, Inc., under NASA contract NAS5-26555.

References

1. J. Krist, *TINY TIM User's Manual Version 4.0*, (Space Telescope Institute, Baltimore, Md., 1994).

2. H. Hasan and C. Burrows, "Telescope Image Modelling," submitted to Pub. Astronomical Society of the Pacific (1994).
3. C. Roddier and F. Roddier, "Combined approach to the Hubble Space Telescope wave-front distortion analysis," *Appl. Opt.* **32**, 2992–3008 (1993).
4. R. W. Gerchberg and W. O. Saxton, "A practical algorithm for the determination of phase from image and diffraction plane pictures," *Optik (Stuttgart)* **35**, 237–246 (1972).
5. C. Burrows, ed., *WFPC2 Instrument Handbook Version 2.0*, (Space Telescope Science Institute, Baltimore, Md., 1994).
6. J. R. Fienup, J. C. Marron, T. J. Schulz, and J. H. Seldin, "Hubble Space Telescope characterized by using phase-retrieval algorithms," *Appl. Opt.* **32**, 1747–1767 (1993).
7. T. Barrett and D. Sandler, "Artificial neural network for the determination of Hubble Space Telescope aberration from stellar images," *Appl. Opt.* **32**, 1768–1774 (1993).
8. C. Burrows, J. Holtzman, S. Faber, P. Bely, H. Hasan, C. Lynds, and D. Schroeder, "The Imaging Performance of the Hubble Space Telescope," *Astrophysical J.* **369**, L21–L25 (1991).
9. "Final report: Hubble Independent Optical Review Panel," Doc. P-442-0078 (Goddard Space Flight Center, Greenbelt, Md., 1992).
10. L. Furey, Memo A16-ST-0316 (Hughes Danbury Optical Systems, Danbury, Conn., 2 May 1994).